Journal of Cluster Science (2023) 34:2901–2918
https://doi.org/10.1007/s10876-023-02436-5

ORIGINAL PAPER

In Silico-DFT Investigation of Nanocluster Alloys of Al-(Mg, Ge, Sn) Coated by Nitrogen Heterocyclic Carbenes as Corrosion Inhibitors

Fatemeh Mollaamin[1] · **Majid Monajjemi**[2]

Received: 1 December 2022 / Accepted: 29 March 2023 / Published online: 15 April 2023

Abstract

Aluminum alloys with magnesium are broadly applied as structural materials for their high ductility and remarkable corrosion resistance. As the strongest alloys of this system have low stability specifications, the present research aims to investigate the probability of making strong of Al–Mg alloy by doping silicon, germanium and tin. This work presents an analysis of the influence of some organic heterocyclic inhibitors owing to Langmuir adsorption and DFT and TD-DFT method with different process parameters, on the corrosion resistance of aluminum alloy containing Al-X–Y (X = Mg, Y = Si, Ge, Sn). The ONIOM approach has been performed with a three-layered level of high by CAM-B3LYP theoretical function using 6–31 + G (2d,p) and LANL2DZ basis sets applying Gaussian 16 revision C.01; a medium semi-active part that consists of essential electronic contributions; and a low level part that has been handled using MM2 force field approaches. The physicochemical properties of inhibitor → metal alloy complexes are evaluated with the Langmuir adsorption through NMR, NBO, UV–VIS, HOMO/LUMO and DOS/PDOS graphs toward structural, electronic and thermodynamic properties and other quantum attributes. The fluctuation of occupancy of natural bond orbitals has been estimated for [pyridine,2-picoline,3-picoline,4-picoline, 2,4-lutidine → Al–Mg–(Si, Ge, Sn)] concerning the influence of nitrogen atom in the benzene ring of related heterocyclic compounds becoming close to the monolayer nanosurface of Al-X–Y (X = Mg, Y = Si, Ge, Sn) alloys. Furthermore, the results of partial electron density states (PDOS) have confirmed an obvious charge accumulation between the Al–Mg alloy and doped atoms of Si, Ge, and Sn through the recognition of the conduction band region. Based on the computed values of UV–VIS spectrums for pyridine, 2-picolone, 3-picoline, 4-picoline and 2,4-lutidine adsorbed on the Al–Mg-Y (Y = Si/Ge/Sn) alloys surface, there are maximum adsorption band wavelengths between 1000 nm and 4000 nm, respectively. In addition, it has been observed the sharpest peak in 2250 nm for all of these inhibitors adsorbed on the Al–Mg-Y (Y = Si/Ge/Sn) alloys surface. This study revealed that appropriate control of the coating process by Langmuir adsorption can illustrate inhibiting the aluminum alloys corrosion through an investigation of their structural, electronic and thermodynamic properties.

Keywords Al-X–Y (X = Mg Y = Si Ge Sn) alloys nanosurface · Langmuir adsorption · ONIOM; CAM-B3LYP/LANL2DZ,6–31 + G(2d,p) · Corrosion inhibitors

Introduction

Aluminum alloys have been the principle compounds applied for airframe structures until the enhancing tendency in the application of composites of the polymer matrix.

Aluminum-magnesium (Al–Mg) alloys are lighter than other aluminum alloys and much less flammable than other alloys consisting of high amounts of magnesium. The magnificent enhancement in resistance at elevated temperature was accomplished after solution treatment through activating settlement becoming hard through Mg possessing phases.

Aluminum–silicon (Al–Si) is one of the most important aluminum alloys with high amounts of silicon in casting and has a large limitation of usages in the aerospace and automotive industries through a best combination of mechanical properties, as well as good wear resistivity and corrosion resistance [1–4].

✉ Fatemeh Mollaamin
smollaamin@gmail.com

[1] Department of Biomedical Engineering, Faculty of Engineering and Architecture, Kastamonu University, Kastamonu, Turkey

[2] Department of Chemical Engineering, Central Tehran Branch, Islamic Azad University, Tehran, Iran

Si element in Al–Si based cast alloys impacts tensile properties at both room and high temperature, but its role becomes more important in lack of alloy elements such as Mg, Fe and Cu [5]. Some elements like Cu and Mg added to Al alloys ameliorate the mechanical attributes and conduct the alloy to reply the heat dealing. The existence of magnesium also increases resistance and reduces the rate of strength loss at high temperature in the alloys.

Al–Mg–Ge alloys are estimated to display identical aging attitude as Al–Mg–Si alloys, so, they have been alternatively employed to analyze precipitates in Al–Mg–Si alloys. However, the interactions between solute atoms and vacancies in Al–Mg–Ge alloys are not vivid. In this study, the physicochemical properties in Al–Mg–Si and Al–Mg–Ge alloys were illustrated using DFT/ONIOM calculations, and the similarities and differences of these parameters in each alloy were analyzed.

Among the various methods that minimize corrosion of metal surface, its inhibition by organic molecules is one of the most applicable methods because of its stability and low cost [6–10]. There are many researches that have been dedicated to the application of efficient heterocyclic and heteroatomic structures including organic compounds that augment the anticorrosion attributes of metal surfaces and alloys. The existence of heteroatoms containing O, S, N, P atoms, aromatic rings and multiple bonds with π-electrons in these inhibitors help extensively to the formation of inactive blocks on metal surface and alloys, so closing the active sites of corrosion [11–16].

The aim of this paper is the use of organic compounds as corrosion inhibitors for aluminum and its alloys. The passive layer is insoluble in aqueous and many organic solutions. There is a positive connection between the thickness of the passive layer and the efficiency of preventing corrosion [17–19].

Because diverse characteristics of organic structures are represented, it is essential that the electrons of a set of organic structures are discussed. Recently, organic solar cells owing to their complete symmetry with the donor polymer have applied efficient fullerene free acceptor molecules accompanying DFT and TD-DFT methods for discovering the photovoltaic and opto-electric attributes of modeling the structures [20–22].

Moreover, reorganizing the electron and hole energies are also estimated with excitation energy. Results of various calculated factors have suggested that these modeled molecules are impressive ingredients for probable usages in the subject of OSCs system [23, 24].

In addition, the scientists have exhibited more end-capped electron-accepting units which are plain and applicable alternative tactics for designing the NFAs group [25, 26].

Therefore, operated organic compounds as corrosion stoppers were chosen and determined on the basis of their physicochemical characteristics [27, 28] and relatively little consideration has been dedicated to the quantitative estimation of the internal and steric influence of these compounds upon their inhibition yield. In other works, it has been studied the interaction between imidazole and the aluminum surface which is often employed in experimental researches [29].

It has been observed that heterocyclic compounds consisting of nitrogen atoms are good corrosion inhibitors for many metals in various acidic media, for instance benzotriazole at the copper and iron electrode, isoquinoline derivatives and imidazole derivatives at the iron electrode which are effective stoppers for corrosion of these metal surfaces [30–46]. In addition, the electron withdrawing thiazole ring was employed as a bridged unit in modeling of the small molecular electron acceptor (DC-IDT2Tz), provided with indacenodithiophene as core and 1,1-dicyanomethylene-3-indanone as end-capped unit, and thiazole ring as spacers [47–49].

The microscopic interaction and reaction mechanism between molecules could be profoundly disclosed from the quantum chemical characteristics, which prepare a beneficial path to find adsorption attitude between molecules and interfaces at the atomic and molecular stages [50–52]. These days, it has been represented that pyridine and its derivatives had been used as corrosion inhibitors of the aluminum electrode [53–55].

Furthermore, the method of carbon adding has become the main industrial grain refinement technique for Mg–Al alloys. In fact, the thermodynamic process of the Al_2MgC_2 carbide makes grain refining of Mg–Al alloys by carbon insemination under optimization procedure using quantitative simulations [56–58].

It has been studied that pyridine family compounds have been broadly applied through their intense polarity and increasing potency in ionic liquids and solution. It is seen that some compounds including nicotine-amide, pyridine-2-formamide and pyridine-4-formamide can be employed as efficient increasing agents for electro-deposition of aluminum in [Bmim] $Cl/AlCl_3$ with the unclear mechanism in finding the intermolecular interaction between additives and electrode, charge distribution, and adsorption comportment [52].

The present work intends to accomplish an extension of the previous work [55] concerning the role of pyridine and its family compounds as corrosion inhibitor for aluminum alloys which have been generated by adding some elements including Si, Ge, and Sn to Al–Mg alloy and forming the Al-X–Y (X = Mg, Y = Si, Ge, Sn) alloys surface. These complexes have been investigated using NMR, IR, UV–Vis spectroscopy and HOMO–LUMO orbital frontier analysis. The choice of a representative of compounds of this class as a potential candidate for a highly effective aluminum alloy

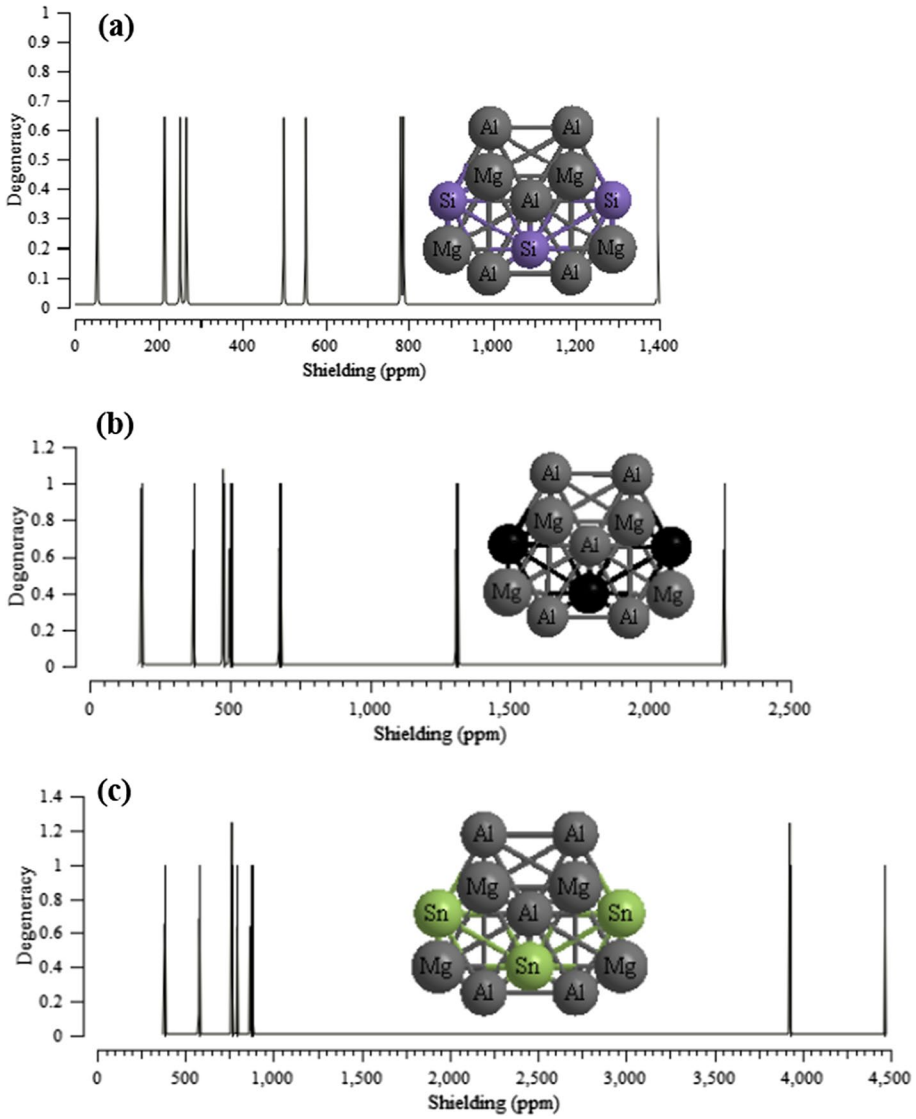

Scheme 1 IR spectrums for aluminum alloys (Al-X–Y) consisting of **a** Al–Mg-Si, **b** Al–Mg-Ge, and **c** Al–Mg–Sn

corrosion inhibitor is reasonable due to its facile synthetic method, low cost and presence of nitrogen heteroatoms containing double bonds in the chemical structure.

Materials and Methods

Aluminum Alloys

Several methods and combinations have been employed to decrease the corrosion of aluminum and its alloys in different environments by that coating of organic, inorganic and even natural inhibitors which are among the most common protection tested methods [59, 60].

The particular components for alloying of aluminum element are copper, magnesium, manganese, silicon, tin, nickel and zinc. Light weight and corrosion resistance of aluminum alloys make them suitable in engineering structures and components.

Alloys of Al–Mg–Si achieve solidity by the precipitation of heavy numbers of nanometer sized, somewhat linked precipitates in the form of needles. At first, a high homogenization or extrusion temperature ensures that most solute atoms exist on Al lattice positions. Then, the lattice gets supersaturated with solute in the room temperature. These atoms will enter into small the clusters on the aluminum lattice. After a short time at the high temperature, appropriate clusters start reorganizing into periodic constructions (Scheme 1a) [11, 61, 62].

Ternary Al alloys of Al–Mg–Si are extendedly applied as car bodies replacing heavier metals related to the economic pressure which needs the decrease of CO_2 emission and fuel consumption. Al–Si alloys without Cu additions are employed when appropriate corrosion resistance is needed. So, Mg is able to replace with Cu. In fact, Mg and

Si can produce the intermetallic hardening phase Mg_2Si which precipitates in the α-aluminum matrix and enhances the efficiency of resistance. The principal restrictions of the ternary alloy of aluminum-magnesium-silicon cast ingredients are because of the remarkable impact of the solidity situations on the final microstructure. The final cast ingredients unavoidably consists of a determined number of defects like oxide films, shrinkage and gas porosity, which impress the exhaustion behavior and the mechanical parameters [63–67].

In some researches, the precipitation in an Al–Mg–Ge alloy has been studied the application of annular dark field scanning TEM (ADF-STEM) and high-resolution transmission electron microscopy (HRTEM). The hardness enhancement is produced by the precipitation of nanometre-sized metastable phases from solid solution during artificial ageing [68].

The fine precipitates had forms including an near-hexagonal network of Ge atoms with sub-cell dimensions a = b ≈ 0.405 nm, c = 0.405 nm which is very identical to the Si network that relates all precipitate constructions in the Al–Mg–Si alloys and its equilibrium phase is β-Mg_2Ge corresponds to its phase diagram. In some investigations, the precipitation sequence of Al–Mg–Ge alloys consisting of various components of Mg_2Ge has been studied by TEM and HRTEM observation and hardness test for finding the impact of Mg_2Ge components on age-hardening treatment of the alloys [69–71].

Doernberg and his coworkers has done the thermodynamic analysis for describing the binary systems for the liquid phase accompanying the solution model containing Al, Mg, Sn and Mg_2Sn as the species [72]. A single ternary interaction parameter was discovered sufficient to match all experimental information. Aluminum (fcc) and magnesium (cph) were defined as disordered substitutional solutions. The allotropic figures of tin and the binary components Mg_2Sn, Mg_2Al_3 (β), and ε phases were behaved as stoichiometric phases [73].

Moreover, the degeneracy of NMR shielding for each compounds has been shown in the maximum range approximately between 50 ppm and 1400 ppm for Al–Mg–Si (Scheme 1a); 200 ppm-2250 ppm for Al–Mg–Ge (Scheme1b); and 350–4500 for Al–Mg–Sn (Scheme 1c) alloys nanosurface.

Then, the NMR parameters of isotropic (σ_{iso}) and anisotropic shielding tensors (σ_{aniso}) for aluminum, silicon, germanium and tin for the ternary alloys of Al–Mg–Si, Al–Ge and All-Mg–Sn participating in interatomic interaction with inhibitors and intra-atomic interaction with themselves have been calculated by using Gaussian 16 revision C.01 program software (Table 1 & Fig. 1) [74].

The quantum chemical calculations yield the chemical shielding (CS) tensors in principal axes system to evaluate

Table 1 NMR properties of σ_{iso} and σ_{aniso} of metal atoms for Al–Mg-X(X = Si, Ge, Sn) alloys surface in ppm

Al–Mg–Si												
ppm	Al1	Mg2	Si3	Mg4	Al5	Mg6	Al7	Si8	Al9	Si10	Mg11	Al12
σ_{iso}	267.85	780.83	246.06	253.02	53.18	787.26	1395.83	207.99	552.13	347.92	215.30	499.04
σ_{aniso}	3285.94	227.54	1048.94	431.79	3640.51	249.96	429.46	2164.58	2564.61	1077.70	491.52	2291.60
Al–Mg–Ge												
ppm	Al1	Mg2	Ge3	Mg4	Al5	Mg6	Al7	Ge8	Al9	Ge10	Mg11	Al12
σ_{iso}	476.51	681.49	1307.62	185.69	476.18	677.05	370.59	2263.47	498.77	1314.21	185.22	504.72
σ_{aniso}	192.76	367.27	2034.53	375.97	193.04	361.54	569.14	770.03	331.92	2028.91	371.59	331.87
Al–Mg–Sn												
ppm	Al1	Mg2	Sn3	Mg4	Al5	Mg6	Al7	Sn8	Al9	Sn10	Mg11	Al12
σ_{iso}	579.17	764.09	3928.04	385.65	580.94	763.99	794.71	4468.80	868.69	3927.92	382.67	879.40
σ_{aniso}	374.38	357.26	2167.90	715.50	368.28	359.39	491.70	892.00	633.74	2162.73	725.81	641.15

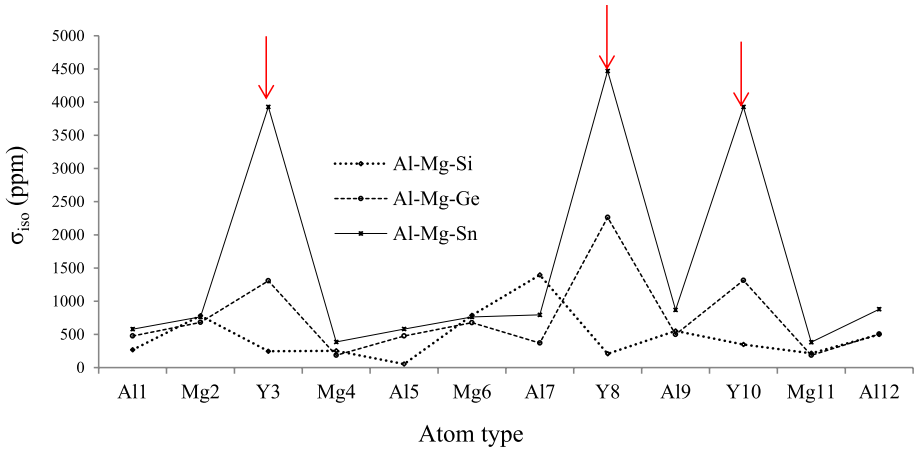

Fig. 1 Isotropic NMR shielding (σ_{iso}) for Al, Mg, Si, Ge, and Sn extracted from Al–Mg–Si, Al–Mg–Ge and Al–Mg-Sn alloys surface (Y = Si/Ge/Sn)

the isotropic chemical-shielding (CSI), and anisotropic chemical-shielding (CSA) [75]:

$$\mathrm{CSI(ppm)} = (\sigma 33 + \sigma 22 + \sigma 11)/3 \quad (1)$$

$$\mathrm{CSA(ppm)} = \sigma 33 - (\sigma 22 + \sigma 11)/2 \quad (2)$$

The calculation of nuclear magnetic resonance (NMR) for chemical shifts for assigning the structural and geometrical of compounds has been accomplished. In fact, Gauge Invariant Atomic Orbital (GIAO) method has been suggested as an accurate method for NMR parameter calculations (Table 1 and Fig. 1).

In fact, it has been represented that the isotropic shielding of silicon, germanium and tin at the ternary alloys of Al–Mg–Si, Al–Ge and All-Mg–Sn which can participate in interatomic interaction with inhibitors and intra-atomic interaction with themselves has the most fluctuation of NMR shielding (Fig. 1).

Corrosion Resistance Increment by Alloy Ingredients

The high corrosion resistance of the Al-alloy is related to a thin but very tight and tightly holding layer of Al oxide produced on the surface of the compound which defends the material against further oxidation. Despite of these attractive properties, in the existence of offensive ions such as chloride and halide, the protective layer might be locally ruined, and a corrosive attack happens [76].

The principal corrosion trouble accompanied with Al and its alloys relates to the localized breakdown of the inactive film which conducts to the start and increase of corrosion cavities in a chloride medium [77].

Aluminum alloys can be susceptible to intergranular corrosion if second-phase micro constituents are formed at grain boundaries. A corrosion potential of the alloy different from that of the matrix will also cause intergranular corrosion. The presence of appreciable amounts of soluble alloying elements such as Cu, Mg, Si, and Zn, will make these alloys susceptible to stress-corrosion cracking [78].

Some of the common types of corrosion for Al which are independent of the corrosive environment consist of pitting, stress-corrosion cracking, exfoliation, intergranular, and galvanic [78]. The non-heat treatable alloys have a higher corrosion resistance toward general corrosion compared to the heat treatable alloys. However, the alloys containing the Al-Mg_2Si system also show considerable resistance to general corrosion. The same behavior is observed for the alloys that do not contain copper (Al–Zn–Mg). The alloys' resistance to pitting corrosion increases significantly with increasing purity [79].

Three-Layer ONIOM Level

In theoretical ONIOM method, any combination of three levels in the reducing order of accuracy can be accepted in ONIOM3. The typically acceptable levels are high (QM1), medium (QM2), and low (QM3or MM), where high level (QM1) often is an ab initio or DFT method, medium level (QM2) is a low-level ab initio, DFT, or semi-empirical (SE) QM method, and low level is an SE QM method or an MM method [80].

In this work, through ONIOM method, QM1 has been launched using the DFT method of CAM-B3LYP with 6–31 + G(2d,p) basis set for carbon and hydrogen atoms and LANL2DZ for some aluminum atoms in the adsorption cites. QM2 has been performed on the nitrogen, carbon and hydrogen in the adsorption sites due to semi-empirical methods. Finally, a QM3 has been considered on the other Al atoms with MM2 force fields (Scheme 2) [80].

So, the mixing of three levels of QM1, QM2 and QM3 in reducing order of accuracy has been assigned containing high, medium, and low levels of theory [80].

$$E_{\mathrm{ONIOM}} = E_{\mathrm{high(QM1)}} + E_{\mathrm{medium(QM2)}} + E_{\mathrm{low(QM3)}} \quad (3)$$

The ONIOM method could be lightly extended and popularized to an n-layer method [81]:

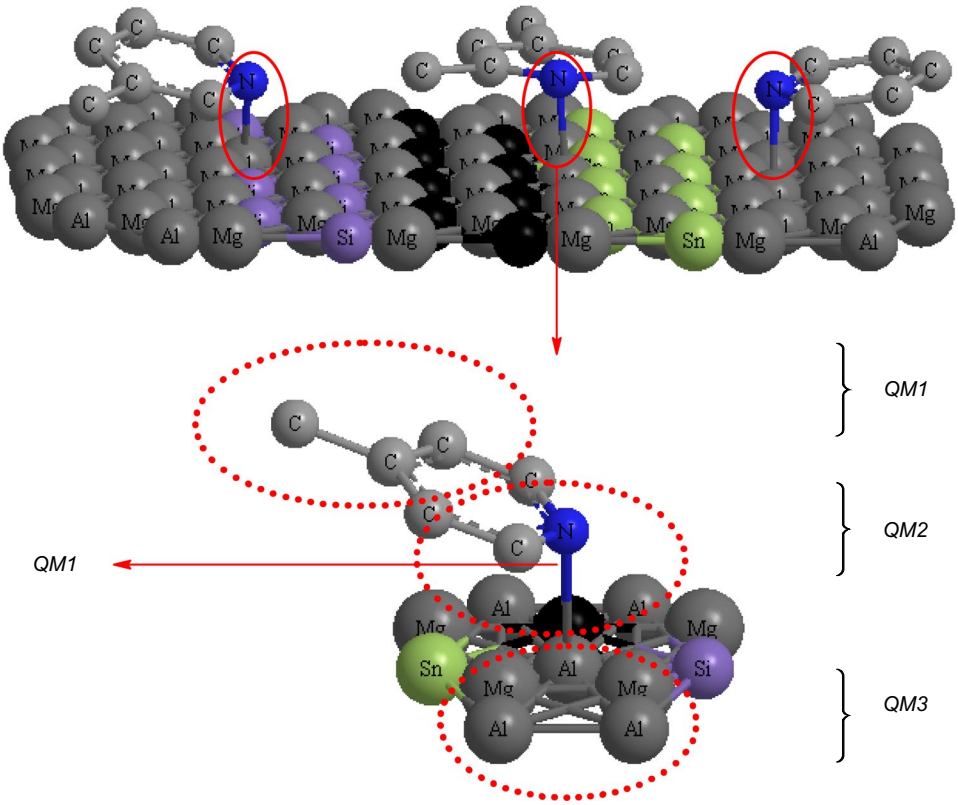

Scheme 2 Process of physical and chemical adsorption of pyridine and its family (2-picolone, 3-picoline, 4-picoline and 2,4-lutidine onto Aluminum surface in different levels containing high, medium and low levels by theoretical ONIOM method of calculation

$$E_{\mathrm{ONIOM}n} = \sum_{i=1}^{n} E[\mathrm{level}(i), model(n+1-i)] - \sum_{i=2}^{n} E[\mathrm{level}(i), model(n+2-i)] \quad (4)$$

The three-layer method ONIOM permits us to investigate a larger system more precisely than the one-layer model which can treat a medium size system very accurately like a huge system with modest accuracy (Scheme 2) [82]. This three-layer model has been employed to activate barriers for the pyridine, 2-picoline, 3- picoline, 4- picoline and 2, 4-lutidine onto mono-layer Al-X–Y (X = Mg, Y = Si, Ge, Sn) surface toward forming the Langmuir adsorption complexes including pyridine → Al–Mg-Si, pyridine → Al–Mg-Ge, pyridine → Al–Mg-Sn; 2-picoline → Al–Mg-Si, 2-picoline → Al–Mg-Ge, 2-picoline → Al–Mg-Sn; 3-picoline → Al–Mg-Si, 3-picoline → Al–Mg-Ge, 3-picoline → Al–Mg-Sn; 4-picoline → Al–Mg–Si, 4-picoline → Al–Mg–Ge, 4-picoline → Al–Mg–Sn; and 2,4- lutidine → Al–Mg–Si, 2,4- lutidine → Al–Mg–Ge, 2,4- lutidine → Al–Mg–Sn (Scheme 2).

Theory of Langmuir Adsorption

The Langmuir adsorption isotherm is applied to characterize the equilibrium between adsorbate and adsorbent structure, where the adsorption system is limited to one molecular layer. In fact, the study of the impact of the organic inhibitors in solution and the nature of the corrosive aluminum alloys on the adsorption bond strength yield information about the mechanism of interaction of the inhibitor with the Al-alloys surface, which in turn Langmuir adsorption isotherms provide excellently. The Langmuir isotherm is widely used in the identification of inhibitor adsorption status specification and it is represented as follows [83]:

$$\frac{C_{inh}}{\theta} = \frac{1}{K_{ads}} + C_{inh} \quad (5)$$

where C_{inh} is the inhibitor concentration; θ is the fractional coverage of the steel surface and K_{ads} is the equilibrium constant of the adsorption & desorption procedures.

Using the Langmuir isotherm, the equilibrium constant of adsorption and desorption procedures (K_{ads}) could be specified and depends on the standard free energy of adsorption ΔG^{o}_{ads} as follows [9]:

$$\Delta G^{o}_{ads} = -RTln\left(55.5K_{ads}\right) \quad (6)$$

where R is the gas constant (8314 J K^{-1} mol^{-1}), T is the absolute temperature (T) and the value 55.55 (mol^{-1})is the concentration of water in solution.

The pyridine, 2-picoloine,3-picoline, 4-picoline and 2,4-lutidine as corrosion inhibitors on the ternary aluminum

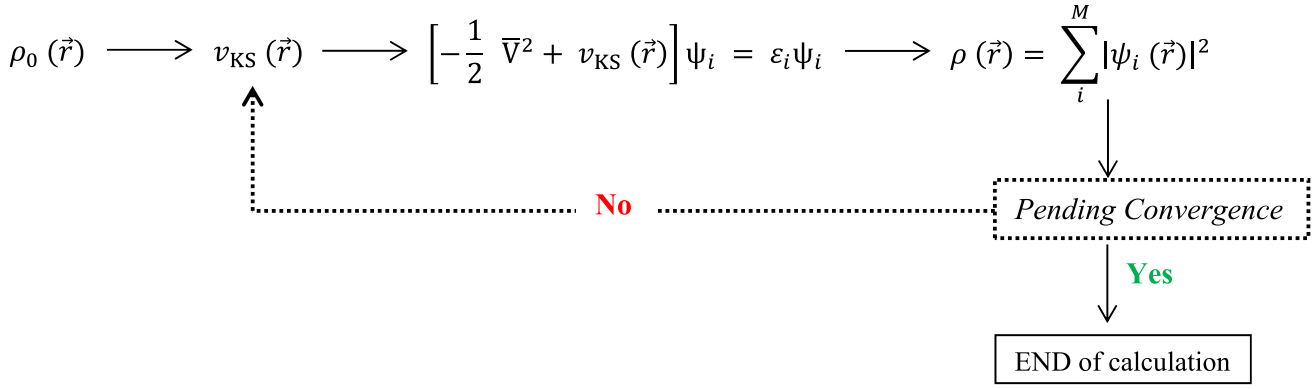

Scheme 3 Process of density functional theory computation within the Kohn–Sham approach

alloys surface containing Al–Mg–Si, Al–Mg–Ge, and Al–Mg–Sn in NaCl solution was assigned by the most suitable Langmuir isotherm, which exhibits the chemisorptive nature of the bond between the inhibitor molecules and the Al-X–Y (X = Mg, Y = Si, Ge, Sn) alloys, the equilibrium distribution of ions of the adsorbing compound between the solid and liquid phases, and a monolayer attribute (Scheme 2).

In Scheme 2, it has been observed that adsorbed molecules are kept on the Al-X–Y (X = Mg, Y = Si, Ge, Sn) alloys with chemisorbed inhibitors having high protection.

Theoretical Method of Density Functional Theory (DFT)

DFT or Density functional theory approaches are the standard and the most employed theoretical methods for electronic structure calculations [84–88]. The appearance of the generalized gradient approximation (GGA) for the exchange–correlation functional increased the DFT accuracy [89] and the foretold molecular structures, relative energies and frequencies are nearly analogous to the second order Møller–Plesset perturbation theory (MP2) method, with notable triumph to behave transition metal clusters [90]. The Hohenberg–Kohn (HK) functions have severely made the electronic density admissible as basic variable to electronic and structure calculations. On the other hand, progress of the practical DFT approaches only became remarkable after W. Kohn and L. J. Sham published their famous set of equations which are represented as Kohn–Sham (KS) equations (Scheme 3) [87].

Using the electronic density within the KS figure lets a significant decrease of the computational request of quantum calculations. Therefore, the KS approach simplifies the path for investigating systems that cannot be studied by conventional ab initio systems.

Kohn and Sham present the solution which uses monoelectronic orbitals to estimate the kinetic energy in a simple and approximately precise, by leaving a residual correction that can be calculated apart. Therefore, one begins with a reference system of M non-interacting electrons subjected to the external potential v_s and with Hamiltonian [87]:

$$\hat{H}_s = -\sum_i^M \frac{1}{2}\overline{V}_i^2 + \sum_i^M v_s(\vec{r}_i) = \sum_i^M \hat{h}_s;\ \hat{h}_s = -\frac{1}{2}\overline{V}_i^2 + v_s(\vec{r}_i) \tag{7}$$

By introducing the single particle orbitals ψ_i, all electronic densities physically acceptable for the system of non-interacting electrons can be written in the form:

$$\rho(\vec{r}) = \sum_i^M |\psi_i(\vec{r})|^2 \tag{8}$$

Finally, the total energy could be calculated by the KS method through the following equation:

$$E[\rho] = \sum_i^M n_i \langle \psi_i \left| -\frac{1}{2}\overline{V}^2 + v_{ext}(\vec{r}) + \frac{1}{2}\int \frac{\rho(\vec{r}')}{|\vec{r} - \vec{r}'|} d\vec{r}' \right| \psi_i \rangle + E_{xc}[\rho] + \frac{1}{2}\sum_\beta^N \sum_{\alpha \neq \beta}^N \frac{Z_\alpha Z_\beta}{|\vec{R}_\alpha - \vec{R}_\beta|} \tag{9}$$

So, the exact exchange energy functional is illustrated by the Kohn–Sham orbitals instead of the density, so it is placed as the indirect density functional. This study has applied the influence of the hybrid functional of three-parameter basis set of B3LYP (Becke, Lee, Yang, Parr) within the framework of DFT upon theoretical calculations [91, 92]. The popular B3LYP (Becke, three-parameter, Lee–Yang–Parr) exchange–correlation functional is [93–95]:

$$E_{XC}^{B3LYP} = (1-\alpha)E_x^{LSDA} + \alpha E_x^{HF} + b\Delta E_x^B + (1-c)E_c^{LSDA} + cE_c^{LYP} \tag{10}$$

where $\alpha = 0.20, b = 0.72, c = 0.81$ is a generalized gradient approximation: the Becke exchange functional [91] and the correlation functional of Lee, Yang and Parr [92] for B3LYP and E_c^{LSDA} is the VWN local spin density approximation to the correlation functional [96].

Density functional theory (DFT) calculations have been performed using Gaussian 16 revision C.01 [74] software. The input files for the corrosion inhibitors adsorbed onto the Al–Mg-Si, Al–Mg–Ge, and Al–Mg–Sn surfaces (Scheme 1) have been prepared with GaussView 6.1 [97] owing to the rigid system and Z-Matrix format of which a blank line has been placed and using LANL2DZ,6–31 + G(2d,p) basis sets to determine chemical shielding, frequencies, occupancy and hybrid of natural atomic orbitals, electrostatic potential, electronic potential, energy gap of frontier orbitals, natural atomic charges, and other quantum properties for this investigation. The rigid PES has been run at CAM-B3LYP/LANL2DZ,6–31 + G(2d,p) for pyridine and its family (2-picoline, 3-picoline, 4-picoline and 2,4-lutidine) adsorbed onto aluminum and its alloys in which the small energy difference between the formations of nitrogen → aluminum complexes can lead us to an appropriate coated surface for ignoring the corrosion. So, it has been explored that the surface binding site preference of N-atom is largely influenced by the presence of neighboring nitrogen atoms. The calculated nitrogen → aluminum pair distribution functions have indicated that the formation of clusters directs to shorter nitrogen → aluminum bond length compared to the homogeneous growth.

Results and Discussion

Natural Bond Orbitals (NBO)

The Natural Bond Orbital (NBO) analysis of pyridine and four derivatives of 2-picoline, 3-picoline, 4-picoline and 2,4-lutidine has illustrated the character of electronic conjugation between bonds in the inhibitor and Al-X–Y (X = Mg, Y = Si, Ge, Sn) alloys nanosurface (Table 2 & Fig. 2).

In Fig. 2, it has been observed the fluctuation of occupancy of natural bond orbitals for pyridine → Al–Mg-Si, pyridine → Al–Mg-Ge, pyridine → Al–Mg-Sn; 2-picoline → Al–Mg-Si, 2-picoline → Al–Mg-Ge, 2-picoline → Al–Mg-Sn; 3-picoline → Al–Mg-Si, 3-picoline → Al–Mg-Ge, 3-picoline → Al–Mg-Sn; 4-picoline → Al–Mg-Si, 4-picoline → Al–Mg-Ge, 4-picoline → Al–Mg-Sn; and 2,4- lutidine → Al–Mg-Si, 2,4- lutidine → Al–Mg-Ge, 2,4- lutidine → Al–Mg-Sn through the Langmuir adsorption process by indicating the active nitrogen atom in heterocyclic compounds becoming close to the nanosurface.

Figure 2 has denoted two sharp graphs which belong to the clusters of 2,4-lutidine → Al–Mg-Si and 2,4-lutidine → Al–Mg-Ge, respectively. Therefore, the interaction between the partially filled d orbital of the metallic fragment (d_{yz} in of metal atoms) and the partially filled π orbital of the N-heterocyclic carbenes causes the simultaneous donation and back-donation interactions. On the other hand, complexes with low d electrons indicate a portion both from π donation and from π back donation; once components with more d electrons are discussed, π back bonding overcomes the interaction of the π orbitals of the N-heterocyclic carbenes with the d orbitals of the metal center in the Al-X–Y (X = Mg, Y = Si, Ge, Sn) alloys nanosheet. This exhibits that the π interactions change the population of the d atomic orbitals in the metal center, which might transfer electron density to the N-heterocyclic carbenes in d^0, or admit electron density in d^{10} metal-doped Al-surface.

Thermodynamic Analysis

In this part, the stability of the metal-doped Al-alloy clusters of N-heterocyclic carbenes has been investigated through thermodynamic properties which define the reactions that

Table 2 NBO analysis for the organic heterocyclic inhibitor containing (pyridine, 2-picoline, 3-picoline, 4-picoline, 2,4-lutidine) → Al-X–Y (X = Mg, Y = Si, Ge, Sn) alloys nanosurface

Inhibitor → metal and metal alloy surface	Bond orbital	Occupancy	Hybrids	$R_{N\text{-}Al}$ (Å)
Pyridine → Al–Mg–Si	BD (1) N1—C2	0.9845	0.7552 ($sp^{2.46}$) N + 0.6555 ($sp^{2.08}$) C	1.9295
2-picoline → Al–Mg–Si	BD (1) N1—C2	0.9851	0.7550 ($sp^{2.44}$) N + 0.6557 ($sp^{2.07}$) C	1.9298
3-picoline → Al–Mg–Si	BD (1) N1—C2	0.9858	0.7588 ($sp^{2.54}$) N + 0.6513 ($sp^{2.10}$) C	1.9298
4-picoline → Al–Mg–Si	BD (1) N1—C2	0.9839	0.7616 ($sp^{2.80}$) N + 0.6480 ($sp^{2.22}$) C	1.9298
2,4-lutidine → Al–Mg–Si	BD (1) N1—C2	0.9881	0.7594 ($sp^{2.04}$) N + 0.6507 ($sp^{1.98}$) C	1.9299
Pyridine → Al–Mg–Ge	BD (1) N1—C2	0.9851	0.7551 ($sp^{2.44}$) N + 0.6556 ($sp^{2.05}$) C	1.9293
2-picoline → Al–Mg–Ge	BD (1) N1—C2	0.9855	0.7549 ($sp^{2.42}$) N + 0.6558 ($sp^{2.05}$) C	1.9297
3-picoline → Al–Mg–Ge	BD (1) N1—C2	0.9848	0.7611 ($sp^{2.45}$) N + 0.6486 ($sp^{2.12}$) C	1.9297
4-picoline → Al–Mg–Ge	BD (1) N1—C2	0.9830	0.7633 ($sp^{2.69}$) N + 0.6460 ($sp^{2.20}$) C	1.9297
2,4-lutidine → Al–Mg–Ge	BD (1) N1—C2	0.9900	0.7493 ($sp^{2.54}$) N + 0.6622 ($sp^{2.01}$) C	1.9296
Pyridine → Al–Mg–Sn	BD (1) N1—C2	0.9852	0.7542 ($sp^{2.41}$) N + 0.6555 ($sp^{1.99}$) C	1.9300
2-picoline → Al–Mg–Sn	BD (1) N1—C2	0.9858	0.7547 ($sp^{2.39}$) N + 0.6561 ($sp^{1.99}$) C	1.9305
3-picoline → Al–Mg–Sn	BD (1) N1—C2	0.9842	0.7677 ($sp^{2.17}$) N + 0.6409 ($sp^{2.13}$) C	1.9302
4-picoline → Al–Mg–Sn	BD (1) N1- C2	0.9782	0.7697 ($sp^{2.50}$) N + 0.6384 ($sp^{2.22}$) C	1.9304
2,4-lutidine → Al–Mg–Sn	BD (1) N1—C2	0.9835	0.7620 ($sp^{2.22}$) N + 0.6476 ($sp^{2.05}$) C	1.9302

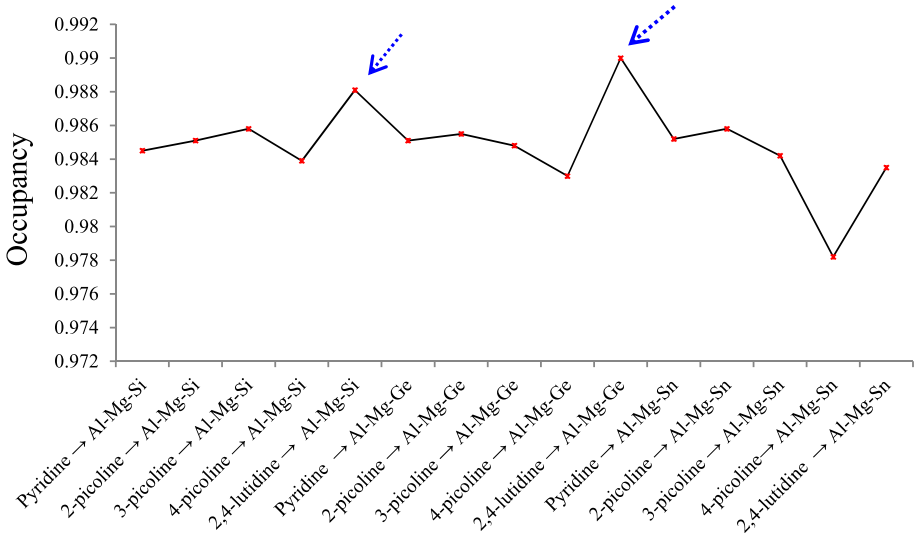

Fig. 2 Occupancy fluctuation extracted of NBO method for the organic heterocyclic inhibitors containing (pyridine, 2-picoline, 3-picoline, 4-picoline, 2,4-lutidine) → Al-X–Y(X = Mg, Y = Si/Ge/Sn) alloys nanosurface

N-heterocyclic carbenes endure in the metal coordination sphere and maybe direct to decomposition of the N-heterocyclic carbenes → metal clusters.

As it has been explained in the previous parts, it has been modeled the several complexes including pyridine → Al–Mg–Si, pyridine → Al–Mg–Ge, pyridine → Al–Mg–Sn; 2-picoline → Al–Mg-Si, 2-picoline → Al–Mg–Ge, 2-picoline → Al–Mg–Sn; 3-picoline → Al–Mg–Si, 3-picoline → Al–Mg–Ge, 3-picoline → Al–Mg-Sn; 4-picoline → Al–Mg-Si, 4-picoline → Al–Mg-Ge, 4-picoline → Al–Mg–Sn; and 2,4- lutidine → Al–Mg-Si, 2,4- lutidine → Al–Mg-Ge, 2,4- lutidine → Al–Mg–Sn. Then, these structures have been computed at CAM-B3LYP level of theory employing 6–31 + G (2d,p) /LANL2DZ basis sets to obtain the more accurate equilibrium geometrical parameters, physical and thermodynamic properties for each of the determined structure containing the distance between nitrogen atom in the benzene ring of the heterocyclic inhibitors and aluminum atom in the Al-X–Y (X = Mg, Y = Si, Ge, Sn) alloys nanosurfaces, dipole moment, ΔE^o, ΔH^o, ΔG^o, S^o, respectively (Table 3).

From Fig. 3, it could be found that the maximum of the Langmuir adsorption isotherm plots based on ΔH_f^o might depend on the interactions between the inhibitor structures and the Al-alloy surfaces. Comparing to ΔH_f^o amounts, it is confirmed a good agreement among calculated results, as well as the correctness of the selected isotherm for the adsorption process of pyridine → Al–Mg-Si, pyridine → Al–Mg-Ge, pyridine → Al–Mg-Sn; 2-picoline → Al–Mg-Si, 2-picoline → Al–Mg-Ge, 2-picoline → Al–Mg-Sn; 3-picoline → Al–Mg-Si, 3-picoline → Al–Mg-Ge, 3-picoline → Al–Mg-Sn; 4-picoline → Al–Mg-Si, 4-picoline → Al–Mg-Ge, 4-picoline → Al–Mg-Sn; and 2,4- lutidine → Al–Mg-Si, 2,4- lutidine → Al–Mg-Ge, 2,4-lutidine → Al–Mg-Sn (Fig. 3).

The adsorptive capacity of inhibitor structures on the Al-alloys surface is approved by the ΔG_{ads}^o amounts.

$$\Delta H_{ads}^o = \Delta H_{f,inh\to Al-X-Y}^o - \left(\Delta H_{f,inh}^o + \Delta H_{f,Al-X-Y}^o\right); \quad X = Mg, Y = Si, Ge, Sn \tag{11}$$

On the basis of data in Table3, it is predicted that the adsorption of the inhibitor on the Al–Mg-Y(Y = Si, Ge, Sn) alloys surface might be physical and chemical nature. As shown in Table3, all the computed ΔH_{ads}^o amounts are very close, which exhibit the agreement of the evaluated data by all methods and the validity of the computations.

Besides, Fig. 4 has illustrated the changes of dipole moment versus the distance among N atom in the benzene ring of the pyridine,2-picoline,3-picoline,4-picoline and 2,4-lutidine with Al atom in the Al-X–Y (X = Mg, Y = Si, Ge, Sn) alloys nanosurfaces. Figure 4 has shown that the cluster of N-heterocyclic carbene of pyridine has the highest fluctuation during adsorption on the Al–Mg–Sn alloy nanosheet through the electron transfer.

In addition, a dipole moment measurement in the process of Langmuir adsorption between nitrogen atom in the benzene ring of the heterocyclic inhibitors and aluminum atom in the Al-X–Y (X = Mg, Y = Si, Ge, Sn) alloys nanosurfaces illustrates the separation of two opposite electrical charges of N and Al atoms (Table 4). In Fig. 4, the dipole moment generated by the difference in the electronegativity of two atoms (N, Al) in complexes (Table 4) based on equation: $\mu = q \cdot r$ has been plotted versus the distance between N and Al atoms in the inhibitors and aluminum alloys, respectively, where μ is the dipole moment, q is the magnitude of the separated charge, and r is the distance between the charges.

Table 3 The Physicochemical properties of adsorption for pyridine, 2-picoline, 3-picoline, 4-picoline and 2,4- lutidine as corrosion inhibitors on the aluminum and its alloys surface including Al–Mg-Si, Al–Mg–Ge and Al–Mg–Sn at 300 K

Structure	$R_{N\rightarrow Al}$ (Å)	μ (Debye)	$\Delta E^o \times 10^{-4}$ (kcal/mol)	$\Delta E^o{}_R \times 10^{-4}$ (kcal/mol)	$\Delta H^o \times 10^{-4}$ (kcal/mol)	$\Delta G^o \times 10^{-4}$ (kcal/mol)	S^o (cal/K. mol)
Al–Mg–Si	–	1.72	− 177.59	–	− 177.59	− 177.59	75.32
Al–Mg–Ge	–	1.53	− 512.93	–	− 512.93	− 512.93	79.09
Al–Mg–Sn	–	2.25	− 124.62	–	− 124.62	− 124.62	79.86
Pyridine	–	2.03	− 15.38	–	− 15.38	− 15.38	68.62
Pyridine → Al–Mg–Si	1.9295	2.47	− 192.95	0.02	− 192.95	− 192.95	91.15
Pyridine → Al–Mg–Ge	1.9293	1.92	− 525.54	2.77	− 525.54	− 525.54	92.17
Pyridine → Al–Mg–Sn	1.93	2.90	− 1261.62	− 1121.00	− 1261.62	− 1261.63	91.69
2-picoline	–	1.74	− 17.81	–	− 17.81	− 17.81	73.69
2-picoline → Al–Mg–Si	1.9298	2.05	− 195.38	0.02	− 195.38	− 195.38	88.76
2-picoline → Al–Mg–Ge	1.9297	1.67	− 527.97	2.77	− 527.97	− 527.98	98.16
2-picoline → Al–Mg–Sn	1.9305	2.85	− 1264.05	− 1121.62	− 1264.05	− 1264.06	94.31
3-picoline	–	2.21	− 17.81	–	− 17.81	− 17.81	73.72
3-picoline → Al–Mg–Si	1.9298	2.80	− 195.40	0.00	− 195.40	− 195.39	88.87
3-picoline → Al–Mg–Ge	1.9297	2.49	− 527.98	2.76	− 527.98	− 527.98	90.87
3-picoline → Al–Mg–Sn	1.9302	3.33	− 1264.06	− 1121.63	− 1264.06	− 1264.07	94.24
4-picoline	–	2.46	− 17.81	–	− 17.81	− 17.81	73.71
4-picoline → Al–Mg–Si	1.9298	3.97	− 195.38	0.02	− 195.38	− 195.38	88.66
4-picoline → Al–Mg–Ge	1.9297	2.87	− 527.97	2.77	− 527.97	− 527.98	92.47
4-picoline → Al–Mg–Sn	1.9304	4.15	− 1264.05	− 1121.62	− 1264.05	− 1264.05	94.97
2,4-lutidine	–	2.16	− 20.251	–	− 20.25	− 20.25	78.73
2,4-lutidine → Al–Mg–Si	1.9299	3.94	− 197.81	0.031	− 197.81	− 197.82	95.00
2,4-lutidine → Al–Mg–Ge	1.9296	2.04	− 530.43	2.751	− 530.43	− 530.43	97.36
2,4-lutidine → Al–Mg–Sn	1.9302	4.23	− 1266.49	− 1121.619	− 1266.49	− 1266.49	94.54

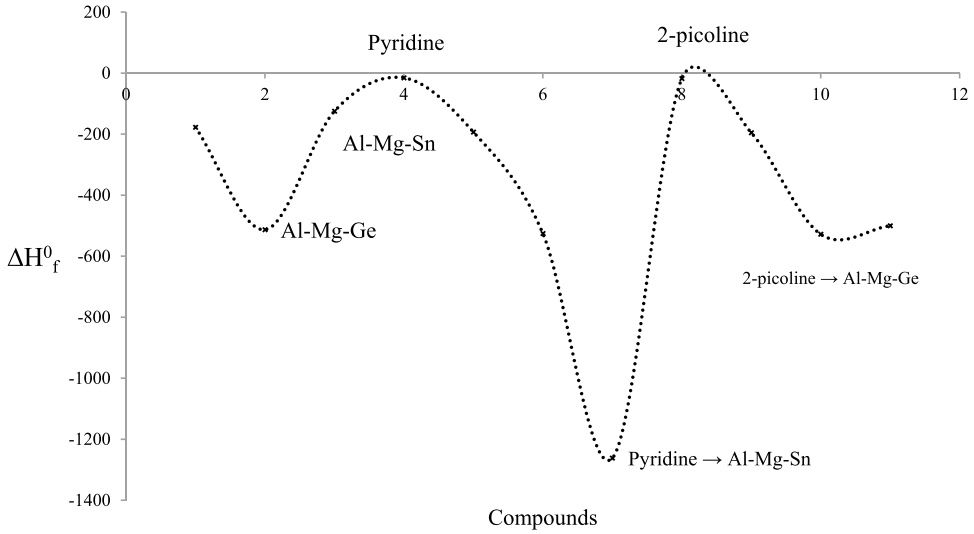

Fig. 3 Changes of ΔH^0_f (kcal/mol) for some inhibitors which are linked to Al-X–Y (X = Mg, Y = Si, Ge, Sn) alloys nano-surface using CAM-B3LYP/LANL2DZ,6–31 + G(2d,p) calculations

The role of cross conjugation in electron donating and also accepting properties by nitrogen atoms in heterocyclic carbenes with metal atoms in Al–Mg-X (X = Si, Ge, Sn) and π-electrons in corrosion inhibition has been seen from DFT computations. The effects of the conjugation by the electron donating group have been explored towards the extent of corrosion protection with a significant resistance. DFT study has unraveled the active centers of N-heterocyclic carbenes which are responsible for electron transfer to metal surface.

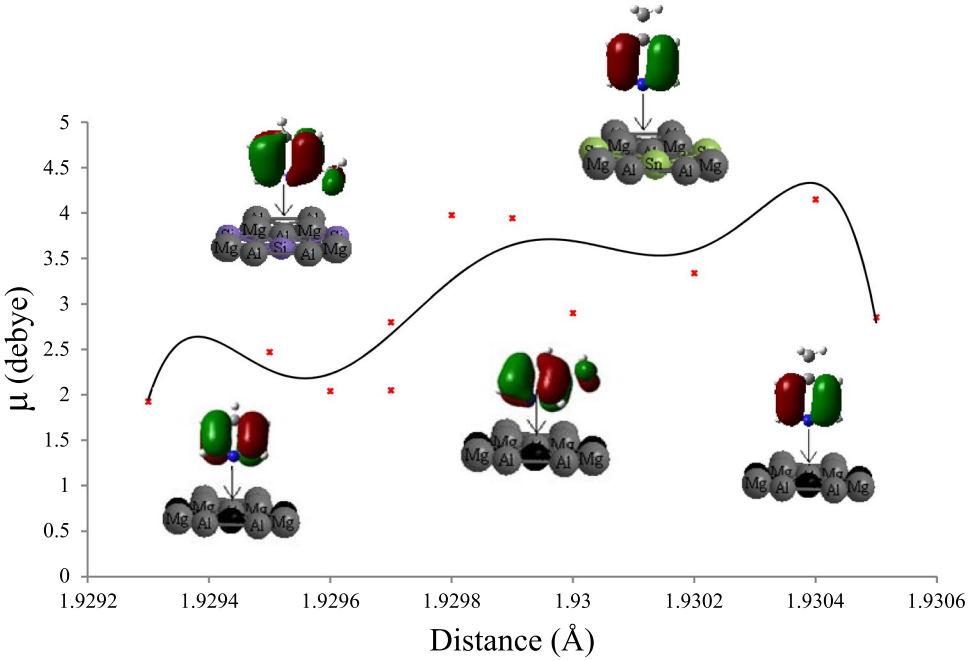

Fig. 4 The changes of Gibbs free energy for adsorption of pyridine and its derivatives as corrosion inhibitors on the aluminum alloys surface including Al–Mg-Si, Al–Mg-Ge and Al–Mg-Sn versus dipole moment (Debye)

Table 4 The HOMO (a.u.), LUMO (a.u.), band energy gap (ΔE /ev) and other quantities (ev) for the organic heterocyclic inhibitors containing (pyridine, 2-picoline, 3-picoline, 4-picoline, 2,4-lutidine) → Al-X–Y(X = Mg, Y = Si, Ge, Sn) structures using CAM-B3LYP/6–31 + G (2d,p), LANL2DZ

Inhibitor → Al-alloy	HOMO	LUMO	ΔE	μ	χ	η	ζ	ψ
Pyridine → Al–Mg-Si	− 0.00850	0.04666	1.5009	0.5192	− 0.5192	0.7505	0.6662	0.1796
Pyridine → Al–Mg–Ge	− 0.0075	0.03160	1.0639	0.3279	− 0.3279	0.5320	0.9398	0.1010
Pyridine → Al–Mg–Sn	− 0.0454	0.02397	1.8876	− 0.2915	0.2915	0.9438	0.5297	0.0450
2− picoline → Al–Mg–Si	− 0.05091	0.19332	6.6458	1.9376	− 1.9376	3.3229	0.1504	0.5649
2− picoline → Al–Mg–Ge	− 0.02223	0.03506	1.5589	0.1745	− 0.1745	0.7794	0.6415	0.0195
2− picoline → Al–Mg–Sn	− 0.02665	0.02406	1.3799	− 0.0352	0.0352	0.6900	0.7246	8.9785
3-picoline → Al–Mg–Si	− 0.00934	0.03944	1.3273	0.4095	− 0.4095	0.6637	0.7533	0.1263
3-picoline → Al–Mg–Ge	− 0.02660	0.02671	1.4506	0.0015	− 0.0015	0.7253	0.6893	1.5511
3-picoline → Al–Mg–Sn	− 0.02121	0.02326	1.2101	0.0279	− 0.0279	0.6050	0.8264	6.4331
4-picoline → Al–Mg–Si	− 0.00273	0.04448	1.2846	0.5680	− 0.5680	0.6423	0.7784	0.2511
4-picoline → Al–Mg–Ge	− 0.07102	0.15782	6.2270	1.1809	− 1.1809	3.1135	0.1606	0.2239
4-picoline → Al–Mg–Sn	− 0.02567	0.03110	1.5448	0.1477	− 0.1477	0.7724	0.6473	0.0141
2,4-lutidine → Al–Mg–Si	− 0.00672	0.04927	1.5235	0.5790	− 0.5790	0.7618	0.6563	0.2200
2,4-lutidine → Al–Mg–Ge	− 0.00460	0.02766	0.8778	0.3137	− 0.3137	0.4389	1.1392	0.1121
2,4-lutidine → Al–Mg–Sn	− 0.03001	0.03489	1.7660	0.0664	− 0.0664	0.8830	0.5662	0.0025

$\Delta E = E_{LUMO} - E_{HOMO}$; $\mu = (E_{HOMO} + E_{LUMO})/2$; $\chi = -(E_{HOMO} + E_{LUMO})/2$; $\eta = (E_{LUMO} - E_{HOMO})/2$; $\zeta = 1/(2\eta)$; $\psi = \mu^2/(2\eta)$

The stability of Al-nanoalloy coated with various N-heterocyclic carbenes has been investigated. An overcoming impact has been seen with a significantly resistance of Al-X–Y (X = Mg, Y = Si, Ge, Sn) alloys nanosurface compared to pure Al-surface [98, 99].

Herein, the stability of N-heterocyclic carbenes belongs to methyl group substituents, double bond between carbons of the ring backbone, which donates aromatic character to that system and electron transferring from nitrogen to metal-doped Al-alloy nanosheet. Figure 4 has observed that the cluster of N-heterocyclic carbene of 2,4-lutidine with two methyl group substituents has the highest diffusion during adsorption on the Al–Mg–Sn nanosheet through the electron transfer.

Frontier Orbitals of HOMO and LUMO

The highest occupied molecular orbital energy (HOMO) and the lowest unoccupied molecular orbital energy (LUMO) have been calculated for

pyridine → Al–Mg-Si, pyridine → Al–Mg-Ge, pyridine → Al–Mg-Sn; 2-picoline → Al–Mg-Si, 2-picoline → Al–Mg-Ge, 2-picoline → Al–Mg-Sn; 3-picoline → Al–Mg-Si, 3-picoline → Al–Mg-Ge, 3-picoline → Al–Mg-Sn; 4-picoline → Al–Mg-Si, 4-picoline → Al–Mg-Ge, 4-picoline → Al–Mg-Sn; and 2,4- lutidine → Al–Mg-Si, 2,4- lutidine → Al–Mg-Ge, 2,4- lutidine → Al–Mg-Sn through the Langmuir adsorption process using CAM-B3LYP/6–31 + G (2d,p), LANL2DZ (Table4).

The HOMO, LUMO and band energy gap (ev) indicated the pictorial explanation of the frontier molecular orbital's which are an important factor for identifying the molecular characteristics of the high coating for aluminum and its alloys against the metal corrosion phenomenon (Table 4).

In other words, the HOMO shows the capability for giving an electron while the LUMO as an electron acceptor exhibits the ability for achieving an electron. Therefore, the energy gap ($\Delta E = E_{LUMO} - E_{HOMO}$) indicates the energy difference between frontier HOMO and LUMO orbital introducing the stability for the structure and unravels the chemical activity of the molecule (Fig. 5).

In this work, energy gap establishes how organic inhibitors (pyridine and its derivatives) interact with the aluminum alloys [Al-X–Y (X = Mg, Y = Si/Ge/Sn)] monolayer surface. Besides, frontier molecular orbitals run an important function in the optical and electrical properties like in UV–Vis spectrums [100]. Moreover, for getting more conclusive approval in identifying the compound characteristics of this structure, a series of chemical reactivity parameters consisting of chemical potential (μ), electronegativity (χ), hardness (η), softness (ζ), electrophilicity index (ψ) has been done (Table 4) [101, 102]. The amounts of the parameters in Table 4 have exhibited a good stability of pyridine and its family compounds through Langmuir adsorption on the monolayer aluminum alloys surface.

The illustration of donor–acceptor molecules depends on the relative frontier molecular levels. The HOMO–LUMO gap defines the charge transfer in organic molecules adsorbed on the Al-alloy surface through simplified molecular-level diagram. In fact, the amount of transferred charges might be considerably small, as in the case of parallel and perpendicular coordination, which indicate electronic couplings smaller than in co-facial coordination. Figure 5 has observed two sharp peaks which belong to the clusters of 2-picoline → Al–Mg-Si and 4-picoline → Al–Mg-Ge, respectively. Figure 5 has indicated the energy level shifts of molecule → surface-HOMO and molecule → surface -LUMO of nanoclusters as a function of their distance *d* orbitals from the high symmetry points of each metal-doped on the Al-surface. Therefore, the HOMO level of molecule is being lowered as it loses its electron, whereas the LUMO level of surface is being raised as it gains partial charge. The value of charge transfer is restricted by the cross spot of these two frontier levels (Table 4 and Fig. 5).

Electronic properties (DOS and PDOS)

The electronic structures of Al–Mg-X (X = Si, Ge, Sn) have been analyzed to simplify subsequent discussion for interfacial electronic properties using DFT/LANL2DZ basis set. The graph of partial DOS (PDOS) has illustrated that the p states of doped- Si, Ge-, and Sn- in the Al–Mg alloy

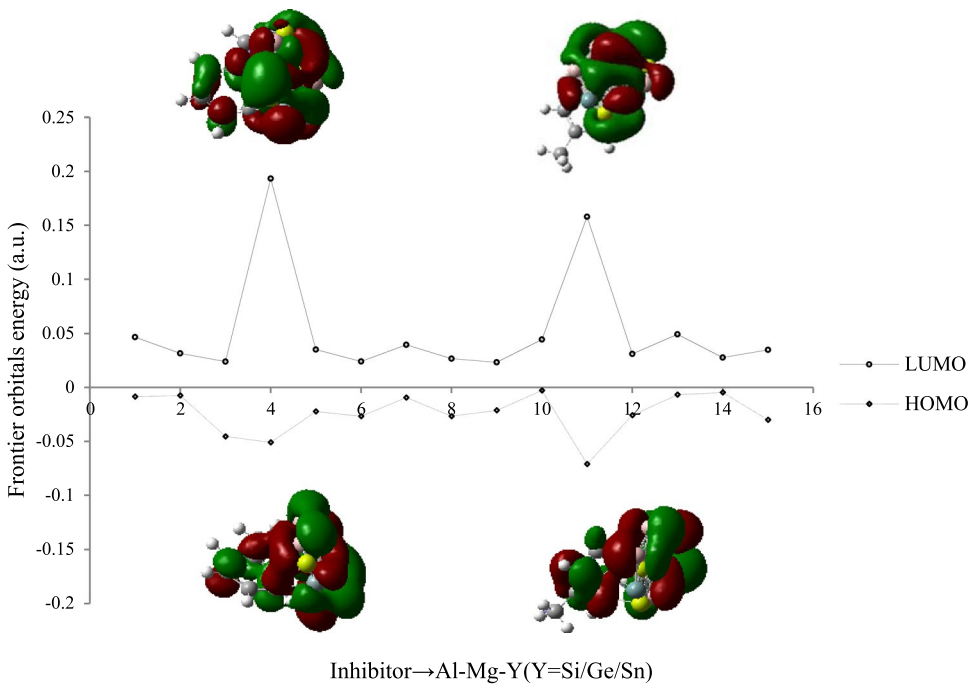

Fig. 5 The energy gap of HOMO/LUMO (a.u.) for adsorbing pyridine, 2-picoline, 3-picoline, 4-picoline and 2,4-lutiding on the Al-X–Y (X = Mg, Y = Si/Ge/Sn) alloys surface

are dominant through the conduction band (Fig. 6a–c). A distinct metallic feature can be observed in the Al–Mg-X (X = Si, Ge, Sn) alloys because of the strong interaction between the *p* states of Al and the *d* state of Ge and Sn near the Fermi energy. Moreover, the existence of covalent features for these alloys has exhibited the identical energy amount and figure of the PDOS for the *p* orbitals of Al and *d* orbitals of Ge and Sn.

Figure 6a has shown that the Si states in the Al–Mg-Si alloy have more contributions at the middle of the conduction band between -5 eV to -15 eV, while contribution of Al sates are expanded and Mg states have minor contributions; Ge states in the Al–Mg-Ge alloy have more contributions at the middle of the conduction band between − 1 eV to − 10 eV, while contribution of Al state are weak and Mg states have the expanded contribution (Fig. 6b); and Sn states in the Al–Mg-Sn alloy reveal the expanded contribution with the conduction band between − 1 eV to − 20 eV, while Al and Mg states have the limited and minor contributions (Fig. 6c).

The results also approved by the partial electron density (PDOS), which have showed a certain charge association between the Al–Mg alloy and doped elements of Si, Ge, Sn. In other words, the Sn states have large contributions in the valence band, while Si states have fewer contributions. Thus, the cluster dominant of non-metallic and metallic features and a certain degree of covalent features can illustrate the increasing of the semiconducting direct band gap of (Si, Ge, Sn)-doped the Al–Mg alloy.

UV–VIS

Time-dependent density functional theory "TD-DFT" is an extension "DFT" which exhibits the equivalency of the time-dependent wave function with the time-dependent electronic density for extracting the efficient potential of an artificial non-interaction model. The most special usage of TD-DFT is in the measurement of excited state energies of isolated systems and solid states which depends on the linear response function indicating how the electron density alters with changing the external potential [103].

In this investigation, TD-DFT/6–31 + G (2d, p), LANL2DZ computations have been also done to identify the low-lying excited states of pyridine, 2-picolone, 3-picoline,4-picoline and 2,4-lutidine adsorbed on the Al-X–Y(X = Mg, Y = Si, Ge, Sn) surface. The results consist of the vertical excitation energies, oscillator strength and wavelength which have been introduced in Fig. 7a–e.

In fact, based on the computed amounts of UV–VIS spectrums for pyridine, 2-picolone, 3-picoline, 4-picoline and 2,4-lutidine adsorbed on the Al–Mg-Y (Y = Si/Ge/Sn) alloys surface, there are maximum adsorption band wavelengths between 1000 nm and 4000 nm, respectively (Fig. 7a–e).

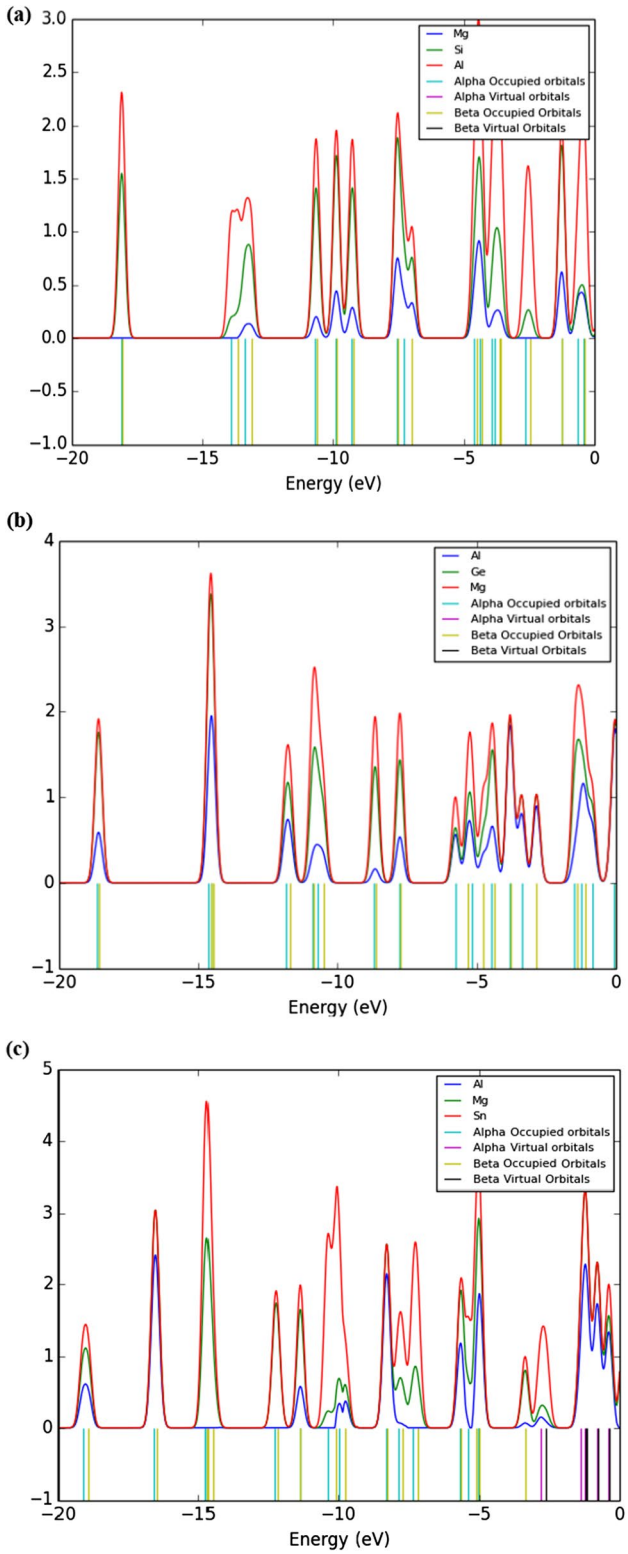

Fig. 6 PDOS of **a** Al–Mg–Si, **b** Al–Mg–Ge and **c** Al–Mg–Sn alloys with Fermi level = 0

Moreover, it has been observed the sharpest peak in 2250 nm for all of these inhibitors adsorbed on the Al–Mg-Y (Y = Si/Ge/Sn) alloys surface (Fig. 7a–e).

Consequently, comparing the three-body physical and chemical properties of Al–Mg–Si, Al–Mg–Ge and Al–Mg–Sn, the Mg-Ge-vacancy interaction in the Al matrix was stronger than the Mg-Si-vacancy interaction. The difference in the bond strength can be illustrated by the difference in the atomic radii against the Al atom. However, the binding energy change with different bond angles was included for the Si and Ge cases. These results exhibit that analogous interactions between inhibitor atoms and vacancies are one of the reasons for the formation of similar adsorption bindings in Al–Mg–Si and Al–Mg–Ge alloys. Furthermore, the potent interactions between inhibitor atoms and vacancies in Al–Mg–Ge alloys suggest that the clustering occurs more rapidly than in Al–Mg–Si alloys, terminating in a speedy increase of hardness at the early step of adsorption.

Conclusion

In this research, the adsorption and diffusion of pyridine and its family on the Al-alloys surface have been investigated based on Langmuir theory using ONIOM method with high, medium and low levels of 6–31 + G(2d,p)/LANL2DZ, semi-empirical and MM2 basis sets, respectively by program package Gaussian 16 revision C.01.

In this work, the efficiency of the organic heterocyclic inhibitors as the aluminum-alloy coating has been studied through the thermoelectric features and characteristics of the environmental condition extracted from NMR, NBO, UV–VIS spectra, HOMO/LUMO frontier orbitals and other quantum data analysis which have been accomplished on pyridine → Al–Mg-Si, pyridine → Al–Mg-Ge, pyridine → Al–Mg-Sn; 2-picoline → Al–Mg-Si, 2-picoline → Al–Mg-Ge, 2-picoline → Al–Mg-Sn; 3-picoline → Al–Mg-Si, 3-picoline → Al–Mg-Ge, 3-picoline → Al–Mg-Sn; 4-picoline → Al–Mg-Si, 4-picoline → Al–Mg-Ge, 4-picoline → Al–Mg-Sn; and 2,4- lutidine → Al–Mg-Si, 2,4- lutidine → Al–Mg-Ge, 2,4- lutidine → Al–Mg-Sn.

An elaborate investigation for the mechanism of local minima in the adsorption potential energy landscape represents that the intact pyridine, 2-picoline, 3-picoline, 4-picoline and 2,4-lutidine are adsorbed with the aromatic ring parallel to the Al–Mg alloy surface. In the preferred path, the these organic inhibitors remain parallel to the surface while performing small single rotational steps with a carbon–carbon double bond hinged above a single aluminum atom in Al–Mg–Si, Al–Mg–Ge, and Al–Mg–Sn. The inhibition properties of the protonated pyridine and derivatives molecules are related to the sum of the net charge and the π charge of the six-ring, respectively. Pyridine and its derivatives have

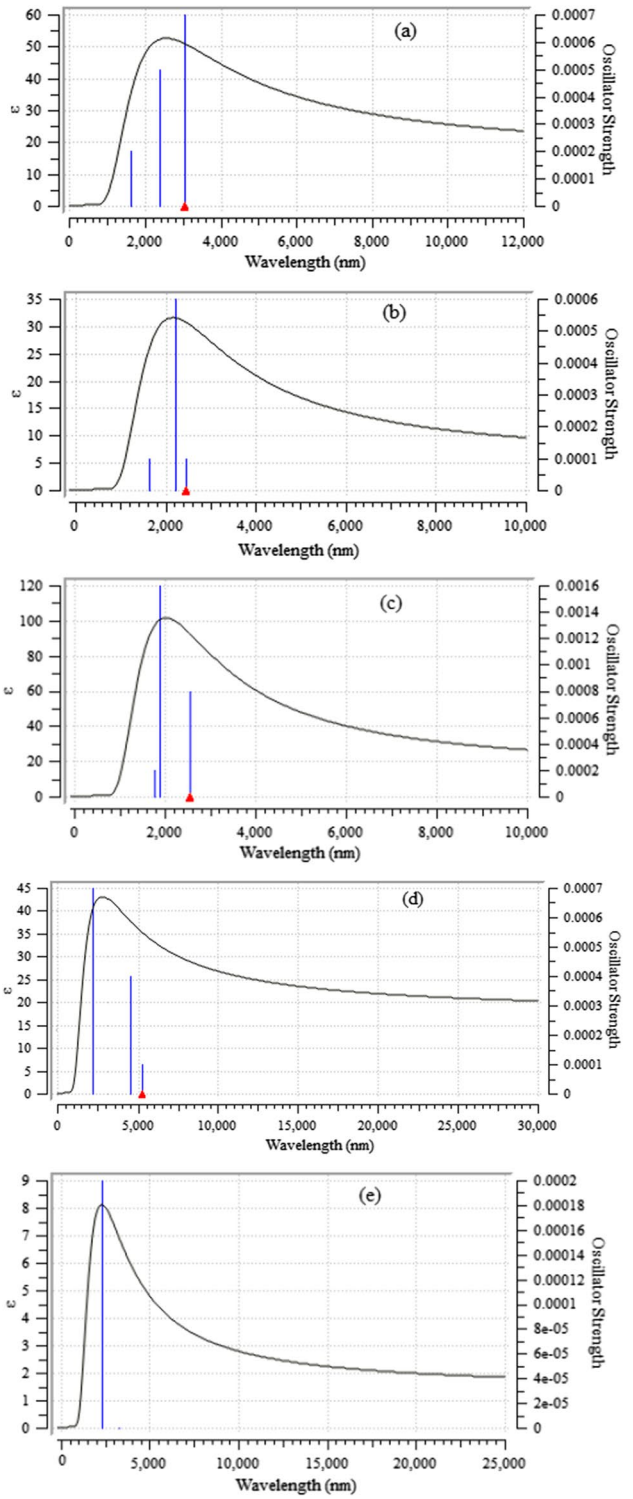

Fig. 7 UV–Vis spectrums for organic heterocyclic inhibitors adsorbing on the aluminum alloys surface using TD-DFT/6–31 + G (2d,p), LANL2DZ including: **a** pyridine → Al–Mg-Y, **b** 2-picoline → Al–Mg-Y, **c)** 3-picoline → Al–Mg-Y, **d** 4-picoline → Al–Mg-Y and **e)** 2,4-lutidine → Al–Mg-Y (Y = Si/Ge/Sn)

been adsorbed on the lattice of the Al–Mg–Si, Al–Mg–Ge, and Al–Mg-Sn electrodes mainly in their protonated forms. The most probable adsorption model of the inhibitors is one in which the N atom of the pyridine ring is close to the aluminum atom of Al–Mg–Si, Al–Mg–Ge, and Al–Mg–Sn in an inclined state.

The authors intend to continue this research focusing on the magnetic properties of nonmagnetic metal-doped SiC monolayer which can be studied by DFT methods. Therefore, different dopants such as Al, Ga, Li, Mg, Na and doping sites are selected and the magnetic treatment will be discussed whether it is observed in Al-, Ga-, Li-, Mg-, and Na-doped system like transition metal (TM) atoms.

References

1. F. Lasagni, A. Lasagni, E. Marks, C. Holzapfel, F. Mücklich, and H. Degischer (2007). *Acta materialia* **55**, 3875–3882.
2. G. Requena, G. Garcés, M. Rodríguez, T. Pirling, and P. Cloetens (2009). *Advanced Engineering Materials* **11**, 1007–1014.
3. Z. Asghar, G. Requena, and F. Kubel (2010). *Materials Science and Engineering: A* **527**, 5691–5698.
4. Y. Wang, R. Guan, D. Hou, Y. Zhang, W. Jiang, and H. Liu (2016). The effects of eutectic silicon on grain refinement in an Al–Si alloy processed by accumulative continuous extrusion forming. *J Mater Sci* **52** (2), 1137–1148.
5. F. Stadler, H. Antrekowitsch, W. Fragner, H. Kaufmann, and P. Uggowitzer (2012). *International Journal of Cast Metals Research* **25**, 215–224.
6. Y. Boughoues, M. Benamira, L. Messaadia, and N. Ribouh (2020). Adsorption and corrosion inhibition performance of some environmental friendly organic inhibitors for mild steel in HCl solution via experimental and theoretical study. *Colloids Surfaces A Physicochem. Eng. Asp.* **593**, 124610. https://doi.org/10.1016/j.colsurfa.2020.124610.
7. Monajjemi, M.; Baie, M.T.; Mollaamin, F. Interaction between threonine and cadmium cation in [Cd(Thr)] (n = 1–3) complexes: Density functional calculations , Russian Chemical Bulletin , 2010, 59. 886–889, https://doi.org/10.1007/s11172-010-0181-5.
8. J. Saranya, M. Sowmiya, P. Sounthari, K. Parameswari, S. Chitra, and K. Senthilkumar (2016). N-heterocycles as corrosion inhibitors for mild steel in acid medium. *J. Mol. Liq.* **216**, 42–52. https://doi.org/10.1016/j.molliq.2015.12.096.
9. T. A. S. Guimarães, et al. (2020). Nitrogenated derivatives of furfural as green corrosion inhibitors for mild steel in HCl solution. *J. Mater. Res. Technol.* **9**, 7104–7122. https://doi.org/10.1016/j.jmrt.2020.05.019.
10. M. Özcan (2008). Interfacial behavior of cysteine between mild steel and sulfuric acid as corrosion inhibitor. *Acta Physico-Chimica Sin.* **24**, 1387–1392. https://doi.org/10.1016/S1872-1508(08)60059-5.
11. F. Mollaamin and M. Monajjemi (2015). Harmonic Linear Combination and Normal Mode Analysis of Semiconductor Nanotubes Vibrations. *J. Comput. Theor. Nanosci* **12**, 1030–1039. https://doi.org/10.1166/jctn.2015.3846.
12. S. A. Ali, M. A. J. Mazumder, M. K. Nazal, and H. A. Al-Muallem (2020). Assembly of succinic acid and isoxazolidine motifs in a single entity to mitigate CO2 corrosion of mild steel in saline media. *Arab. J. Chem.* **13**, 242–257. https://doi.org/10.1016/j.arabjc.2017.04.005.
13. H. Amar, J. Benzakour, A. Derja, D. Villemin, and B. Moreau (2003). A corrosion inhibition study of iron by phosphonic acids in sodium chloride solution. *J. Electroanal. Chem.* **558**, 131–139. https://doi.org/10.1016/S0022-0728(03)00388-7.
14. M. S. El-Sayed (2011). Corrosion and corrosion inhibition of aluminum in Arabian Gulf seawater and sodium chloride solutions by 3-amino-5- mercapto-1,2,4-triazole. *Int. J. Electrochem. Sci.* **6**, 1479–1492.
15. E. S. Sherif (2014). A comparative study on the electrochemical corrosion behavior of iron and X-65 steel in 4.0 wt % sodium chloride solution after different exposure intervals. *Molecules* **19**, 9962–9974. https://doi.org/10.3390/molecules19079962.
16. Yang D, Zhang M, Zheng J, Castaneda H. 2015 Corrosion inhibition of mild steel by an imidazolium ionic liquid compound: the effect of pH and surface pre-corrosion. RSC Adv. 5, 95 160–95 170. (doi:10.1039/ C5RA14556B).
17. M. Finšgar and I. Milošev (2010). Inhibition of copper corrosion by 1,2,3-benzotriazole: A review. *Corrosion Science*. **52** (9), 2737–2749. https://doi.org/10.1016/j.corsci.2010.05.002.
18. A. Y. Shen, S. N. Wu, and C. T. Chiu (1999). Synthesis and Cytotoxicity Evaluation of some 8-Hydroxyquinoline Derivatives. *Journal of Pharmacy and Pharmacology.* **51** (5), 543–548. https://doi.org/10.1211/0022357991772826.
19. CABASSI, PAJ (November–December, et al. (1983). "The improved flotation of gold from the residues of Orange Free State ores" (PDF). *Journal of the South African Institute of Mining and Metallurgy.* **83** (11), 270–276.
20. F. Mollaamin, M. Monajjemi, S. Salemi, and M. T. Baei (2011). A Dielectric Effect on Normal Mode Analysis and Symmetry of BNNT Nanotube. *Fuller. Nanotub. Carbon Nanostructures* **19**, 182–196. https://doi.org/10.1080/15363831003782932.
21. M. Haroon and M. R. S. A. Janjua (2022). Exploring the effect of end-capped modifications of carbazole-based fullerene-free acceptor molecules for high-performance indoor organic solar cell applications. *J Comput Electron* **21**, 40–51. https://doi.org/10.1007/s10825-021-01838-w.
22. Muhammad Ramzan Saeed Ashraf. Janua (2022). Photovoltaic properties and enhancement in near-infrared light absorption capabilities of acceptor materials for organic solar cell applications: A quantum chemical perspective via DFT. *Journal of Physics and Chemistry of Solids.* **171**, 110996. https://doi.org/10.1016/j.jpcs.2022.110996.
23. Asif Mahmood, Ahmad Irfan, and Jin-Liang. Wang (2022). Machine learning and molecular dynamics simulation-assisted evolutionary design and discovery pipeline to screen efficient small molecule acceptors for PTB7-Th-based organic solar cells with over 15% efficiency. *J. Mater. Chem. A.* **10** (8), 4170–4180. https://doi.org/10.1039/D1TA09762H.
24. Muhammad Haroon, Abdulaziz Aaadi, Muhammad Ramzan Saeed Ashraf Janjua 2022 Insights into end-capped modifications effect on the photovoltaic and optoelectronic properties of S-shaped fullerene-free acceptor molecules: A density functional theory computational study for organic solar cells. 35(4): 4314. https://doi.org/10.1002/poc.4314.
25. Asif Mahmood, Jing Yang, Hu. Junyi, Xiaochen Wang, Ailing Tang, Yanfang Geng, Qingdao Zeng, and Erjun Zhou (2018). Introducing Four 1,1-Dicyanomethylene-3-indanone End-Capped Groups as an Alternative Strategy for the Design of Small-Molecular Nonfullerene Acceptors. *J. Phys. Chem. C* **122** (51), 29122–29128. https://doi.org/10.1021/acs.jpcc.8b09336.
26. Asif Mahmood and Jin-Liang. Wang (2021). A time and resource efficient machine learning assisted design of non-fullerene small molecule acceptors for P3HT-based organic solar cells and green

solvent selection. *J. Mater. Chem. A* **9** (28), 15684–15695. https://doi.org/10.1039/D1TA04742F.
27. N. Hackerman and A. C. Makrides (1954). *Ind. Engng. Chem.* **46**, 523.
28. K. Aramaki, N. Hackerman, and J. Eleclrochem (1968). *Soc* **115**, 1007.
29. J. V. Barth, H. Brune, G. Ertl, and R. J. Behm (1990). Scanning tunneling microscopy observations on the reconstructed Au(111) surface: Atomic structure, long-range superstructure, rotational domains, and surface defects. *Phys. Rev. B.* **42**, 9307–9318.
30. Mollaamin, F.; Monajjemi, M. Doping of Graphene Nanostructure with Iron, Nickel and Zinc as Selective Detector for the Toxic Gas Removal: A Density Functional Theory Study. *C* **2023**, *9(1)* , 20. https://doi.org/10.3390/c9010020.
31. M. Monajjemi, M. Khaleghian, N. Tadayonpour, and F. Mollaamin (2010). The effect of different solvents and temperatures on stability of single-walled carbon nanotube: A QM/MD study. *Int. J. Nanosci.* **09**, 517–529.
32. M. Monajjemi, H. Baheri, and F. Mollaamin (2011). A percolation model for carbon nanotube-polymer composites using the Mandelbrot-Given. *Journal of Structural Chemistry* **52**, 54–59. https://doi.org/10.1134/S0022476611010070.
33. W. Kohn and L. J. Sham (1965). Self-Consistent Equations Including Exchange and Correlation Effects. *Phys. Rev.* **140**, A1133–A1138.
34. M. Monajjemi, L. Mahdavian, F. Mollaamin, and M. Khaleghian (2009). Interaction of Na, Mg, Al, Si with carbon nanotube (CNT): NMR and IR study. *Russ. J. Inorg. Chem* **54**, 1465–1473. https://doi.org/10.1134/S0036023609090216.
35. C. Hartwigsen, S. Goedecker, and J. Hutter (1998). Relativistic separable dual-space Gaussian pseudopotentials from H to Rn. *Phys. Rev. B* **58**, 3641–3662.
36. J. P. Perdew, K. Burke, and M. Ernzerhof (1996). Generalized Gradient Approximation Made Simple. *Phys. Rev. Lett.* **77**, 3865–3868.
37. J. VandeVondele and J. Hutter (2007). Gaussian basis sets for accurate calculations on molecular systems in gas and condensed phases. *J. Chem. Phys.* **127**, 114105-1–114105-9.
38. F. Mollaamin and M. Monajjemi (2023). Graphene Embedded with Transition Metals for Capturing Carbon Dioxide: Gas Detection Study Using QM Methods. *Clean Technol.* **5** (1), 403–417. https://doi.org/10.3390/cleantechnol5010020.
39. M. Mavrikakis, P. Stoltze, and J. K. Nørskov (2000). Making gold less noble. *Catal. Lett.* **64**, 101–106.
40. A. Dal Corso (2013). Ab initio phonon dispersions of transition and noble metals: effects of the exchange and correlation functional. *J. Phys. Condens. Matter.* **25**, 145401–145410.
41. E. M. Sarasia, S. Afsharnezhad, B. Honarparvar, F. Mollaamin, and M. Monajjemi (2011). Theoretical study of solvent effect on NMR shielding tensors of luciferin derivatives. *Phys Chem Liquids* **49**, 561–571. https://doi.org/10.1080/00319101003698992.
42. M. A. A. Zadeh, H. Lari, L. Kharghanian, E. Balali, R. Khadivi, H. Yahyaei, F. Mollaamin, and M. Monajjemi (2015). Density Functional Theory Study and Anti-Cancer Properties of Shyshaq Plant. In View Point of Nano Biotechnology. *Journal of Computational and Theoretical Nanoscience.* **12**, 4358–4367.
43. H. Yildirim, T. Greber, and A. Kara (2013). Trends in Adsorption Characteristics of Benzene on Transition Metal Surfaces: Role of Surface Chemistry and van der Waals Interactions. *J. Phys. Chem. C* **117**, 20572–20583.
44. A. Tahan, F. Mollaamin, and M. Monajjemi (2009). Thermochemistry and NBO analysis of peptide bond: Investigation of basis sets and binding energy. *Russian Journal of Physical Chemistry A* **83**, 587–597.
45. M. Hoefling, F. Iori, S. Corni, and K. E. Gottschalk (2010). The Conformations of Amino Acids on a Gold(111) Surface. *ChemPhysChem.* **11**, 1763–1767.
46. K. Bakhshi, F. Mollaamin, and M. Monajjemi (2011). Exchange and Correlation Effect of Hydrogen Chemisorption on Nano V(100) Surface: A DFT Study by Generalized Gradient Approximation (GGA). *Journal of Computational and Theoretical Nanoscience* **8**, 763–768. https://doi.org/10.1166/jctn.2011.1750.
47. Muhammad Ramzan Saeed Ashraf. Janjua (2020). How Does Bridging Core Modification Alter the Photovoltaic Characteristics of Triphenylamine-Based Hole Transport Materials? *Theoretical Understanding and Prediction.* **27** (12), 4197–4210. https://doi.org/10.1002/chem.202004299.
48. Asif Mahmood, Hu. Junyi, Ailing Tang, Fan Chen, Xiaochen Wang, and Erjun Zhou (2018). A novel thiazole based acceptor for fullerene-free organic solar cells. *Dyes and Pigments.* **149**, 470–474. https://doi.org/10.1016/j.dyepig.2017.10.037.
49. Muhammad Ramzan Saeed Ashraf. Janjua (2021). Prediction and Understanding: Quantum Chemical Framework of Transition Metals Enclosed in a B12N12 Inorganic Nanocluster for Adsorption and Removal of DDT from the Environment. *Inorg. Chem.* **60** (14), 10837–10847. https://doi.org/10.1021/acs.inorgchem.1c01760.
50. H. Valencia, M. Kohyama, S. Tanaka, and H. Matsumoto (2009). Ab initio study of EMIM-BF4 crystal interaction with a Li (100) surface as a model for ionic liquid/Li interfaces in Li-ion batteries. *J. Chem. Phys.* **131**, 244705.
51. J. Clarke-Hannaford, M. Breedon, A. S. Best, and M. J. Spencer (2019). The interaction of ethylammoniumtetrafluoroborate [EtNH3+][BF4−] ionic liquid on the Li (001) surface, towards understanding early SEI formation on Li metal. *Phys. Chem. Chem. Phys.* **21**, 10028–10037.
52. Q. Q. Zhang, *Study on Electrodeposition of Aluminum and Aluminum Alloy in Ionic Liquid* (University of Chinese Academy of Sciences, Beijing, China, 2014).
53. B. Cordero, V. Gómez, A. E. Platero-Prats, M. Revés, J. Echeverría, E. Cremades, F. Barragán, and S. Alvarez (2008). Covalent radii revisited. *Dalton Trans.* **21**, 2832–2838.
54. A. van der Bondii (1964). *Waals Volumes and Radii. Phys. Chem.* **68**, 441–451.
55. M. Monajjemi, F. Mollaamin, M. R. Gholami, H. Yoosbashizadeh, S. K. Sadrnezhad, and H. Passdar (2003). Quantum Chemical Parameters of Some Organic Corrosion Inhibitors, Pyridine, 2-Picoline 4-Picoline and 2, 4- Lutidine, Adsorption at Aluminum Surface in Hydrocholoric and Nitric Acids and Comparison Between Two Acidic Media. *Main Group Met. Chem.* **26**, 349–362.
56. M. Suresh, A. Srinivasan, K. R. Ravi, U. T. S. Pillai, and B. C. Pai (2011). Microstructural Refinement and Tensile Properties Enhancement of Mg–3Al Alloy Using Charcoal Additions. *Mater. Sci. Eng. A.* **528** (6), 2502–2508.
57. Y. Huang, K. U. Kainer, and N. Hort (2011). Mechanism of Grain Refinement of Mg–Al Alloys by SiC Inoculation. *Scripta Mater.* **64** (8), 793–96 23.
58. H. L. Wang, J. J. Tang, Y. J. Zhao, and J. Du (2015). First-Principles Study of Mg/Al2MgC2 Heterogeneous Nucleation Interfaces. *Appl. Surf. Sci.* **355**, 1091–1097.
59. T. G. Harvey (2013). Cerium-based conversion coatings on aluminium alloys: a process review. *Corros. Eng. Sci. Technol.* **48** (4), 248–269.
60. N. Chaubey, Savita, et al. (2016). Corrosion inhibition performance of different bark extracts on aluminium in alkaline solution. *J Assoc Arab Univ Basic Appl Sci*. https://doi.org/10.1016/j.jaubas.2015.12.003.
61. Fatemeh Mollaamin, Alireza Ilkhani, Neda Sakhaei, Behnaz Bonsakhteh, Afsaneh Faridchehr, Sogand Tohidi, and Majid

Monajjemi (2015). Thermodynamic and solvent effect on dynamic structures of nano bilayer-cell membrane: Hydrogen bonding study. *Journal of Computational and Theoretical Nanoscience* **12**, 3148–3154. https://doi.org/10.1166/jctn.2015.4092.
62. M. Monajjemi, J. Najafpour, and F. Mollaamin (2013). $(3,3)_4$ Armchair carbon nanotube in connection with PNP and NPN junctions: Ab Initio and DFT-based studies. *Fullerenes Nanotubes and Carbon Nanostructures* **21**, 213–232. https://doi.org/10.1080/1536383X.2011.597010.
63. J. Hu, W. Zhang, D. Fu, J. Teng, and H. Zhang (2019). Improvement of the mechanical properties of Al–Mg–Si alloys with nano-scale precipitates after repetitive continuous extrusion forming and T8 tempering. *Journal of Materials Research and Technology* **8** (6), 5950–5960. https://doi.org/10.1016/j.jmrt.2019.09.070.
64. J. Hu, J. Teng, X. Ji, D. Fu, W. Zhang, and H. Zhang (2017). Enhanced mechanical properties of an Al–Mg–Si alloy by repetitive continuous extrusion forming process and subsequent aging treatment. *Mater Sci Eng A* **695**, 35–44.
65. X. Ji, H. Zhang, S. Luo, F. Jiang, and D. Fu (2016). Microstructures and properties of Al–Mg–Si alloy overhead conductor by horizontal continuous casting and continuous extrusion forming process. *Mater Sci Eng A*. **649**, 128–134.
66. X. Sauvage, E. V. Bobruk, M. Y. Murashkin, Y. Nasedkina, N. A. Enikeev, and R. Z. Valiev (2015). Optimization of electrical conductivity and strength combination by structure design at the nanoscale in Al–Mg–Si alloys. *Acta Mater* **98**, 355–366.
67. L. Mei, X. P. Chen, G. J. Huang, and Q. Liu (2019). Improvement of mechanical properties of a cryorolled Al–Mg–Si alloy through warm rolling and aging. *J Alloys Compd* **777**, 259–263.
68. R. Bjørge, C. D. Marioara, S. J. Andersen, and R. Holmestad (2010). Precipitation in Two Al-Mg-Ge Alloys. *Metallurgical and Materials Transactions A* **41**, 1907–1916. https://doi.org/10.1007/s11661-010-0301-8.
69. Tomoatsu Murakami, Kenji Matsuda, Takeshi Nagai, Junya Nakamura, Tokimasa Kawabata, and Susumu Ikeno (2011). Aging Behavior of Al-Mg-Ge Alloys with Different Mg_2Ge Contents. *Advanced Materials Research* **409**, 63–66. https://doi.org/10.4028/www.scientific.net/AMR.409.63.
70. R. Bjorge, P. Nakashima, C. Marioara, S. Andersen, B. Muddle, J. Etheridge, and R. Holmestad (2011). Precipitates in an Al-Mg-Ge alloy studied by aberration-corrected scanning transmission electron micrscopy. *Acta Materialia* **59** (15), 6103–6109. https://doi.org/10.1016/j.actamat.2011.06.021.
71. K. Kurihara, I. Lobzenko, T. Tsuru, and A. Serizawa (2022). Interactions between solute atoms and vacancies in Al-Mg-X (X = Si, Ge) alloys. *Journal of Japan Institute of Light Metals* **72** (7), 427–429. https://doi.org/10.2464/JILM.72.427.
72. E. Doernberg, A. Kozlov, and R. Schmid-Fetzer (2007). Experimental Investigation and Thermodynamic Calculation of Mg-Al-Sn Phase Equilibria and Solidification Microstructures. *J. Phase Equilib. Diffus.* **28** (6), 523–535.
73. V. Raghavan (2011). Al-Mg-Sn (Aluminum-Magnesium-Tin). *J. Phase Equilib. Diffus.* **32**, 57–60. https://doi.org/10.1007/s11669-010-9798-1.
74. Frisch, M. J.; Trucks, G. W.; Schlegel, H. B.; Scuseria, G. E.; Robb, M. A.; Cheeseman, J. R.; Scalmani, G.; Barone, V.; Petersson, G. A.; Nakatsuji, H.; et.al. Gaussian 16, Revision C.01, Gaussian, Inc., Wallingford CT, 2016.
75. A. K. Fry, K. D. Kwon, S. Komarneni, J. D. Kubicki, and K. T. Mueller (2006). Solid-State NMR and Computational Chemistry Study of Mononucleotides Adsorbed to Alumina. *Langmuir.* **22**, 9281–9286.
76. Kliški´c, M.; Radoševi´c, J.; Gudi´c, S.; Katalini´c, V. Aqueous extract of Rosmarinusofficinalis L. as inhibitor of Al-Mg alloycorrosion in chloride solution. J. Appl. Electrochem. 2000, 30, 823–830.
77. S. S. A. Rehim, H. H. Hassan, and M. A. Amin (2004). Chronoamperometric studies of pitting corrosion of Al and (Al-Si) alloys by halide ions in neutral sulphate solutions. *Corros. Sci.* **46**, 1921–1938.
78. Davis, J.R., 2000. Corrosion: Understanding the Basics. ASM International.
79. R. Winston Revie, *Uhlig's Corrosion Handbook*, 3rd ed. (John Willey & Sons Inc., New York, 2011).
80. Ming-Dao,L., Lu-An, Y.,Qing-Yu, W., Xiao-Ci ,Y., Xiao-Dong, Y.,Jin-Yun, Z.,J.of Chinese Society of Corrosion and Protection.1996;16:3:195.
81. P. Sokkar, E. Boulanger, W. Thiel, and E. Sanchez-Garcia (2015). *J Chem Theory Comput*. https://doi.org/10.1021/ct500956u.
82. Felix Brandt and Christoph R. Jacob (2022). Systematic QM Region Construction in QM/MM Calculations Based on Uncertainty Quantification. *Journal of Chemical Theory and Computation* **18** (4), 2584–2596. https://doi.org/10.1021/acs.jctc.1c01093.
83. M. E. Mashuga, L. O. Olasunkanmi, and E. E. Ebenso (2017). Experimental and theoretical investigation of the inhibitory effect of new pyridazine derivatives for the corrosion of mild steel in 1M HCl. *J. Mol. Struct.* **1136**, 127–139. https://doi.org/10.1016/j.molstruc.2017.02.002.
84. N. Argaman, G. Makov, and J. Am (2000). *Phys.* **68**, 69.
85. H. Chermette (1998). *Coord. Chem. Rev.* **180**, 699.
86. H. Chermette (1999). *J. Comput. Chem.* **20**, 129.
87. W. Kohn, A. D. Becke, and R. G. Parr (1996). Density Functional Theory of Electronic Structure. *J. Phys. Chem.* **100**, 12974–12980. https://doi.org/10.1021/jp960669l.
88. A. C. Q. Ladeira, V. S. T. Ciminelli, H. A. Duarte, M. C. M. Alves, and A. Y. Ramos (2001). *Geochim. Cosmochim. Acta* **65**, 1211.
89. S. F. Sousa, P. A. Fernandes, and M. J. Ramos (2007). *J. Phys. Chem. A* **111**, 10439.
90. W. Koch and M. C. Holthausen, *A Chemist's Guide to Density Functional Theory* (Wiley-VCH, New York, 2001).
91. A. D. Becke (1993). Density-functional thermochemistry. III. The role of exact exchange. *J Chem Phys* **98**, 5648–5652.
92. C. Lee, W. Yang, and R. G. Parr (1988). Development of the Colle-Salvetti correlation-energy formula into a functional of the electron density. *Phys Rev B* **37**, 785–789.
93. K. Kim and K. D. Jordan (1994). Comparison of Density Functional and MP2 Calculations on the Water Monomer and Dimer. *J. Phys. Chem.* **98** (40), 10089–10094. https://doi.org/10.1021/j100091a024.
94. P. J. Stephens, F. J. Devlin, C. F. Chabalowski, and M. J. Frisch (1994). Ab Initio Calculation of Vibrational Absorption and Circular Dichroism Spectra Using Density Functional Force Fields. *J. Phys. Chem.* **98** (45), 11623–11627. https://doi.org/10.1021/j100096a001.
95. C. J. Cramer (2004). "Essentials of Computational Chemistry: Theories and Models, 2nd Edition Wiley". Wiley.com. Retrieved 2021–06–24.
96. S. H. Vosko; L. Wilk; M. Nusair (1980). "Accurate spin-dependent electron liquid correlation energies for local spin density calculations: a critical analysis". Can. J. Phys. 58 (8): 1200–1211. Bibcode:1980CaJPh..58.1200V. doi:https://doi.org/10.1139/p80-159.
97. GaussView, Version 6.06.16, Dennington, Roy; Keith, Todd A.; Millam, John M. Semichem Inc., Shawnee Mission, KS, 2016.
98. Mollaamin F.; Shahriari, S.; Monajjemi,M.; Khalaj, Z. Nanocluster of Aluminum Lattice via Organic Inhibitors Coating: A Study of Freundlich Adsorption. *Journal of Cluster Science* **2022**, 1–16. https://doi.org/10.1007/s10876-022-02335-1.

99. F. Mollaamin and M. Monajjemi (2023). Molecular modelling framework of metal-organic clusters for conserving surfaces: Langmuir sorption through the TD-DFT/ONIOM approach. *MOLECULAR SIMULATION* **49** (4), 365–376. https://doi.org/10.1080/08927022.2022.2159996.
100. J. Aihara (1999). Reduced HOMO−LUMO Gap as an Index of Kinetic Stability for Polycyclic Aromatic Hydrocarbons. *J. Phys. Chem. A* **103** (37), 7487–7495. https://doi.org/10.1021/jp990092i.
101. R. G. Parr and R. G. Pearson (1983). Absolute Hardness: Companion Parameter to Absolute Electronegativity. *J. Am. Chem. Soc.* **105**, 7512–7516. https://doi.org/10.1021/ja00364a005.
102. P. Politzer and F. Abu-Awwad (1998). A comparative analysis of Hartree-Fock and Kohn-Sham orbital energies. *Theor. Chem. Acc* **99**, 83–87. https://doi.org/10.1007/s002140050307.
103. Giovanni Vignale (2008). Real-time resolution of the causality paradox of time-dependent density-functional theory. *Physical Review A*. **77** (6), 062511. https://doi.org/10.1103/PhysRevA.77.062511.